



HAL
open science

Symmetry and couplings in stationary von Kármán Sodium dynamos

Jean Boisson, Sébastien Aumaître, Nicolas Bonnefoy, Mickaël Bourgoïn,
François Daviaud, Bérengère Dubrulle, Philippe Odier, Jean-François Pinton,
Nicolas Plihon, Gautier Verhille

► **To cite this version:**

Jean Boisson, Sébastien Aumaître, Nicolas Bonnefoy, Mickaël Bourgoïn, François Daviaud, et al..
Symmetry and couplings in stationary von Kármán Sodium dynamos. *New Journal of Physics*, 2012,
14, pp.013044. 10.1088/1367-2630/14/1/013044 . hal-00941499

HAL Id: hal-00941499

<https://hal.science/hal-00941499>

Submitted on 13 Apr 2015

HAL is a multi-disciplinary open access archive for the deposit and dissemination of scientific research documents, whether they are published or not. The documents may come from teaching and research institutions in France or abroad, or from public or private research centers.

L'archive ouverte pluridisciplinaire **HAL**, est destinée au dépôt et à la diffusion de documents scientifiques de niveau recherche, publiés ou non, émanant des établissements d'enseignement et de recherche français ou étrangers, des laboratoires publics ou privés.

Symmetry and couplings in stationary Von Kármán sodium dynamos

This article has been downloaded from IOPscience. Please scroll down to see the full text article.

2012 New J. Phys. 14 013044

(<http://iopscience.iop.org/1367-2630/14/1/013044>)

View [the table of contents for this issue](#), or go to the [journal homepage](#) for more

Download details:

IP Address: 140.77.240.96

The article was downloaded on 24/01/2012 at 11:32

Please note that [terms and conditions apply](#).

Symmetry and couplings in stationary Von Kármán sodium dynamos

J Boisson^{1,6}, S Aumaitre¹, N Bonnefoy², M Bourgoïn^{3,4},
F Daviaud¹, B Dubrulle¹, Ph Odier³, J-F Pinton³, N Plihon³
and G Verhille^{3,5}

¹ SPEC/IRAMIS/CEA Saclay and CNRS (URA 2464), 91191 Gif-sur-Yvette Cedex, France

² CEA/CE Cadarache, DER/STR/LTTS, 13108 St Paul lez Durance Cedex, France

³ Laboratoire de Physique de l'École Normale Supérieure de Lyon, CNRS and Université de Lyon, 46 allée d'Italie, 69364 Lyon Cedex 7, France

⁴ Laboratoire des Écoulements Géophysiques et Industriels, CNRS and Université Joseph Fourier, BP 53, 38041 Grenoble Cedex 9, France

⁵ Institut de Recherche sur les Phénomènes Hors Equilibre, UMR CNRS 6594, Aix Marseille Université, BP146, 13384 Marseille Cedex 13, France

E-mail: jeanboisson@gmail.com

New Journal of Physics **14** (2012) 013044 (18pp)

Received 5 October 2011

Published 23 January 2012

Online at <http://www.njp.org/>

doi:10.1088/1367-2630/14/1/013044

Abstract. We study different types of stationary dynamos observed in the Von Kármán sodium (VKS) experiment when varying the electromagnetic boundary conditions on (and in) the impellers. The flow is driven with two impellers made of soft iron (Monchaux *et al* 2007 *Phys Rev. Lett.* **98** 044502) or using one soft-iron impeller and one stainless steel impeller. The magnetic field is mapped using 40 three-dimensional probes distributed within the flow and its surroundings. Symmetry and coupling properties are then retrieved from direct probe measurements and/or from the field structure as reconstructed using the inversion procedure described by Boisson and Dubrulle (2011 *New J. Phys.* **13** 023037). Several salient results are obtained: (i) dynamo action is not achieved unless at least one iron impeller is rotating, at a frequency larger than 15 Hz; (ii) the resulting dynamo is a dipolar, mostly axisymmetric structure; and (iii) the self-sustained magnetic field properties depend on the sodium flow structure between the two impellers. We propose to interpret the stationary dynamos generation as the (constructive or destructive) superposition of two

⁶ Author to whom any correspondence should be addressed.

one-impeller fluid dynamos generated close to the soft-iron impellers, nonlinearly coupled through the turbulent flow, as suggested by Verhille *et al* (2010 *New J. Phys.* **12** 033006). The normal form equation describing this coupling is similar to the one obtained in a theoretical model (Pétréris *et al* 2009 *Phys. Rev. Lett.* **102** 144503).

Contents

1. Introduction	2
2. Experimental setup	3
3. Properties of the stationary dynamos	5
3.1. Parameter space	5
3.2. Threshold	6
3.3. Symmetries	8
3.4. Dipole self-similarity with the distance to the threshold	9
3.5. Geometry of the dynamo mode at $\epsilon = (R_m - R_{m_c})/R_{m_c} = 0.2$	9
4. Discussion and conclusion	12
Acknowledgments	17
References	17

1. Introduction

The Von Kármán sodium (VKS) experiment is an experimental sodium facility designed for studying turbulent dynamos. Since the first observation of a stationary dynamo [1], various dynamical regimes have been reported and analyzed, ranging from reversals [2, 3] to oscillations [4, 6] and bursts [5]. In the present paper, we focus on stationary regimes, with an emphasis on understanding the role of the symmetries and the couplings involved in the dynamo generation process. In most of the experiments reported so far, the fluid is stirred by two iron impellers, resulting in the generation of highly turbulent motion, with a strong mean flow. Kinematic numerical simulations using this mean (axisymmetric) flow have shown that it is able to sustain dynamo action from $R_m \simeq 130$, this threshold being lowered to $R_m = 43$ in the presence of a layer of sodium at rest [10], and to $R_m = 32$ if the ferromagnetic boundary conditions at the impellers are taken into account [11, 15]. The corresponding neutral mode is non-axisymmetric and corresponds to an $m = 1$ equatorial dipole. More refined numerical simulations, taking into account non-axisymmetric fluctuations, have shown the possibility of selecting an axisymmetric neutral mode, in the form of either an $m = 0$ axial dipole or $m = 0$ quadrupole [11, 13, 14]. Theoretical explanations involve coupling between an α -mechanism in the impellers vicinity [11, 12, 25, 26] and either the azimuthal differential rotation or an ω -effect in the vicinity of the impeller enhanced by a jump in magnetic permeability between the rotating impellers and the fluid [7]. In the first case, one can consider that the dynamo is fully ‘fluid’: the fluid is the source of the two elementary steps of the dynamo process. In the second case, the dynamo is semi-fluid: the fluid itself is the source of only one elementary step (the α -effect), while the second step is due to the coupling between the fluid motion and the (low magnetic diffusivity) solid body rotating impeller (an ‘enhanced’ ω -effect). One could even consider that the dynamo process is fully solid (only generated by the two rotating ferromagnetic

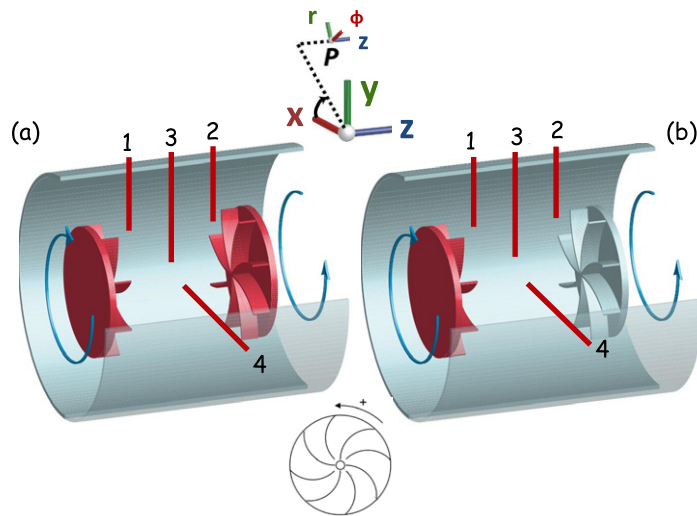


Figure 1. Schematic view showing the experimental configurations and the locations of the magnetic probes. (a) two soft-iron impellers (configuration I–IV); (b) one soft-iron impeller and one stainless steel impeller (configuration V–VIII).

impellers), the fluid in between the two impellers being only a current-carrying medium. In order to select among these three possibilities, we analyze two different recent VKS runs, with different impeller configurations. These two configurations are described in section 2. We then describe and compare the different stationary dynamos observed in these two runs. We show that the fluid motions are essential for the generation of a stationary dynamo, in contrast with recent models that take into account only the impeller composition [13]. We then discuss a picture of the VKS dynamo, based on the hydrodynamic (destructive or constructive) coupling of two semi-fluid (or fluid) dynamos.

2. Experimental setup

The experimental setup of the configurations is schematized in figure 1. In both cases, a von Kármán swirling flow is generated in a copper cylinder (inner radius $R = 289$ mm, outer radius $R_c = 335$ mm and length $H = 604$ mm) by two counter-rotating impellers 371 mm apart (figure 1). In contrast with previous VKS runs [1–6], in the configurations discussed here, there is no shell of stationary sodium around the moving sodium. In all configurations, the impellers are made of discs (radius $R_{\text{imp}} = 154.5$ mm) fitted with eight curved blades with height $h = 41.2$ mm. Their rotation rate can be adjusted independently to (F_1, F_2) (in Hz). The direction of rotation of the impellers indicated by the arrows in figure 1, defined as $F_1, F_2 > 0$, corresponds to the case when the curved blades are counter-rotating and ‘unscoping’ the fluid (pushing the fluid with the convex side of the blades). We denote this regime by 2D(+) in the following, while we use the notation 2D(–) for the $F_1, F_2 < 0$ regime. For some configurations (configurations I–IV, left of figure 1), the two impellers are made of soft iron. They are denoted by I/I. In the other configurations (configurations V–VIII), the left impeller is made of soft iron, while the right impeller is made of stainless steel—these configurations are denoted by I/S. Finally, the configurations with one impeller at rest are denoted by 1D.

Table 1. Summary of all the impellers, rotation regimes and measurement devices recently performed in the VKS experiment.

Configuration name	Impeller 1/impeller 2	Freq 1/Freq 2	Available probes
I (2D(+)) I/I	Iron/iron	> 0/ > 0	1–4
II (2D(–)) I/I	Iron/iron	< 0/ < 0	1–4
III (1D(+)) I/I	Iron/iron	= 0/ > 0	1–4
IV (1D(–)) I/I	Iron/iron	= 0/ < 0	1–4
V (2D(+)) I/S	Iron/stainless steel	> 0/ > 0	1–4
VI (2D(–)) I/S	Iron/stainless steel	< 0/ < 0	1 and 2
VII (1D(+)) I/S	Iron/stainless steel	> 0/ = 0	1–4
VIII (1D(–)) I/S	Iron/stainless steel	< 0/ = 0	1–4

The various configurations described in the present paper are summarized in table 1. The fluid is liquid sodium (density $\rho = 930 \text{ kg m}^{-3}$, electrical conductivity $\sigma = 9.6 \times 10^6 \text{ } (\Omega \text{ m})^{-1}$ and kinematic viscosity $\nu = 6.7 \times 10^{-7} \text{ m}^2 \text{ s}^{-1}$, at 120°C). The driving motor power is 300 kW. Cooling by oil circulation inside the wall of the outer copper vessel allows experimental operation at constant temperature in the range $110\text{--}140^\circ\text{C}$.

We define two non-dimensional control parameters:

- The rotation number $\theta = (F_1 - F_2)/(F_1 + F_2)$, which characterizes the symmetry of the forcing.
- The magnetic Reynolds number $R_m = K \mu_0 \sigma 2\pi R R_{\text{imp}} F$, which estimates the effects magnetic advection on magnetic diffusion. Here, F is the mean forcing frequency $F = (F_1 + F_2)/2$; μ_0 is the magnetic permeability of vacuum; σ is the electrical conductivity of sodium; and $K = A^\pm(1 + |\theta|)$ is a non-dimensional factor describing the efficiency of the impellers as measured in a water experiment through maximal velocities achieved in the vessel [9]. For impellers rotating in the (+) direction ($F > 0$), we measured $A^+ = 0.8$, while $A^- = 0.96$ for impellers rotating in the (–) direction ($F < 0$) [8]. This R_m definition is in agreement with [1, 5]; the definition used in [6] is recovered when letting $A^\pm = 1$, but it misses the 20% efficiency increase of the (–) case. With the present definition, $F_1 = F_2 = 16 \text{ Hz}$ or $F_1 = 16 \text{ Hz}$; $F_2 = 0$ at 120°C gives $R_m = 32$ in the (+) case with $R = 206 \text{ mm}$ (as in [5]) and $R_m = 45$ with $R = 289 \text{ mm}$ (as in this paper). Note that the conductivity of sodium is quite sensitive to temperature variations. These variations are taken into account in the computation of R_m . The magnetic field is measured with the Hall probe arrays partly inserted inside the fluid, as shown in figure 1. The three components of the magnetic field are probed along ten locations spaced by 28 mm, starting at $r = 63 \text{ mm}$ in the midplane and $r = 113 \text{ mm}$ closer to the impellers. Thus, the probes SM1 and SM2, on the one hand, and SM3 and SM4, on the other, have, respectively, six and eight sensors out of ten inside the fluid. The magnetic probe array has been built with Hall effect sensors Sentron 2SA10. Available probe measurements in each configuration are summarized in table 1. For configurations where all probes are available, we have applied the Galerkin reconstruction method introduced in [21] to estimate the global magnetic field properties.

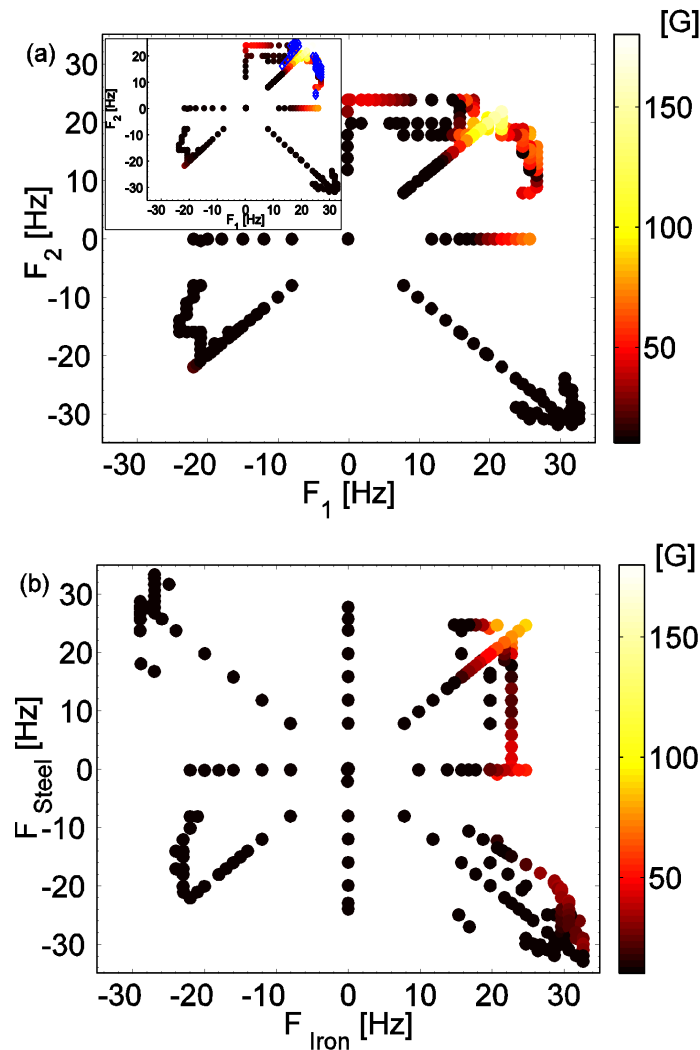


Figure 2. (a) Configurations I–IV, parameter space: mean magnetic field per sensor (in gauss) as a function of F_1 and F_2 . Inset: location of the dynamical regimes (blue diamonds) in the parameter space. (b) Configurations V–VIII; parameter space: mean magnetic field per sensor (in gauss) as a function of $F_1 = F_{\text{iron}}$ and $F_2 = F_{\text{Steel}}$. Note that in these configurations, we did not observe any dynamical regimes.

3. Properties of the stationary dynamo

3.1. Parameter space

The parameter space of configurations I–VIII is represented in figure 2. The color code follows the mean magnetic intensity $B_m = \sqrt{\langle B^2 \rangle}$, where $\langle \cdot \rangle$ is an average over the magnetic arrays 1 and 2 (when available) and the overline denotes a time average of the magnetic field, after the saturated state is reached, over a measurement time of at least 60 s—in order to compute a converged average. The color scale has been chosen to emphasize the dynamo

regimes. One observes several domains of dynamo actions for I/I impellers (figure 2(a)): around $F_1 = F_2 > 14$ Hz (2D(+)) I/I dynamo, around $F_1 = F_2 < -20$ Hz (2D(-)) I/I dynamo and around $F_1 > 18$, $F_2 = 0$ Hz or $F_2 > 20$, $F_1 = 0$ Hz (1D I/I dynamo). The 2D(+), 2D(-) and 1D dynamos are all stationary. When the system evolves from the 2D(+) dynamo to the 1D dynamo, we have observed several interesting dynamical regimes, similar to those described in [2, 3, 5, 6]. The location of such regimes in the parameter space is represented with blue diamonds in the inset of figure 2(a). However, here, we do not investigate these regimes. When one iron impeller is replaced by a stainless steel one (figure 2(b)), several dynamo domains disappear: there is neither 2D(-) dynamo nor 1D dynamo when the stainless steel impeller is rotating. On the other hand, when dynamo action is preserved (1D dynamo with rotating iron impeller, 2D(+) dynamo) the mean magnetic field intensity is about 1.5 smaller than with two iron impellers. Moreover, we did not detect any dynamical regimes (bursts, intermittent dynamo, reversals) in the parameter space region between the 2D(+) and the 1D dynamo domains. Finally, we observed a low-intensity stationary dynamo around $F_1 = 30$, $F_2 = -25$ Hz (co-rotating dynamo), which was not observed with two rotating iron impellers. These observations point out the crucial role played by the iron impellers, since there is no dynamo unless at least one is rotating. However, the co-rotation regimes show that this is not a sufficient condition for dynamo action: two co-rotating iron impellers might ‘neutralize’ each other and produce no dynamo or increase the threshold (in the explored R_m range). To investigate these puzzling observations in more detail, we now focus on the stationary dynamos only, i.e. the 2D(+), 2D(-) and 1D dynamos.

3.2. Threshold

3.2.1. Methodology. In order to compare the different dynamos in different configurations, we plot in figure 3 the mean magnetic energy per unit of mass $E_m = \langle \overline{B^2} \rangle / (\rho \mu_0)$ as a function of R_m . In the 2D(+) and (-) cases, we use the measurements recorded at the two probes close to the impellers (SM1 and SM2), and in the 1D(+) and (-) cases, we use only the probe close to the rotating impeller (SM1 when $F_2 = 0$ Hz and SM2 when $F_1 = 0$ Hz). Here, $\langle \cdot \rangle$ denotes an average over the ten magnetic sensors of the probe and the overline denotes a time average over the measurement time (typically 60–300 s). In the cases when self-generation is reached, one observes a linear increase of the magnetic energy above threshold. An extrapolation of this linear behavior through the R_m axis yields the dynamo threshold R_{m_c} , as reported in table 2.

3.2.2. Role of iron impellers and coupling. In figure 3, the filled symbols correspond to iron impeller(s), while the open symbols correspond to stainless steel one(s). Comparing filled and open symbols with the same color on this plot, one sees that in both the 2D(+) and 2D(-) cases, the dynamo with two iron impellers is more intense than the dynamo with one iron and one steel impeller. This is an indication that in the (+) and (-) regimes the two iron impellers have constructive coupling. Note that in contrast, in other experimental runs not discussed here where the co-rotating regime was explored ($F_1 > 0$, $F_2 < 0$ Hz), no dynamo was observed with two iron impellers, while there was a low-intensity dynamo with one iron and one steel impeller. This is suggestive of a nonlinear destructive coupling process.

3.2.3. Role of ferromagnetic boundary conditions and flow structure. When only one iron impeller is rotating, there is no dynamo in the (-) cases in the explored R_m range (see

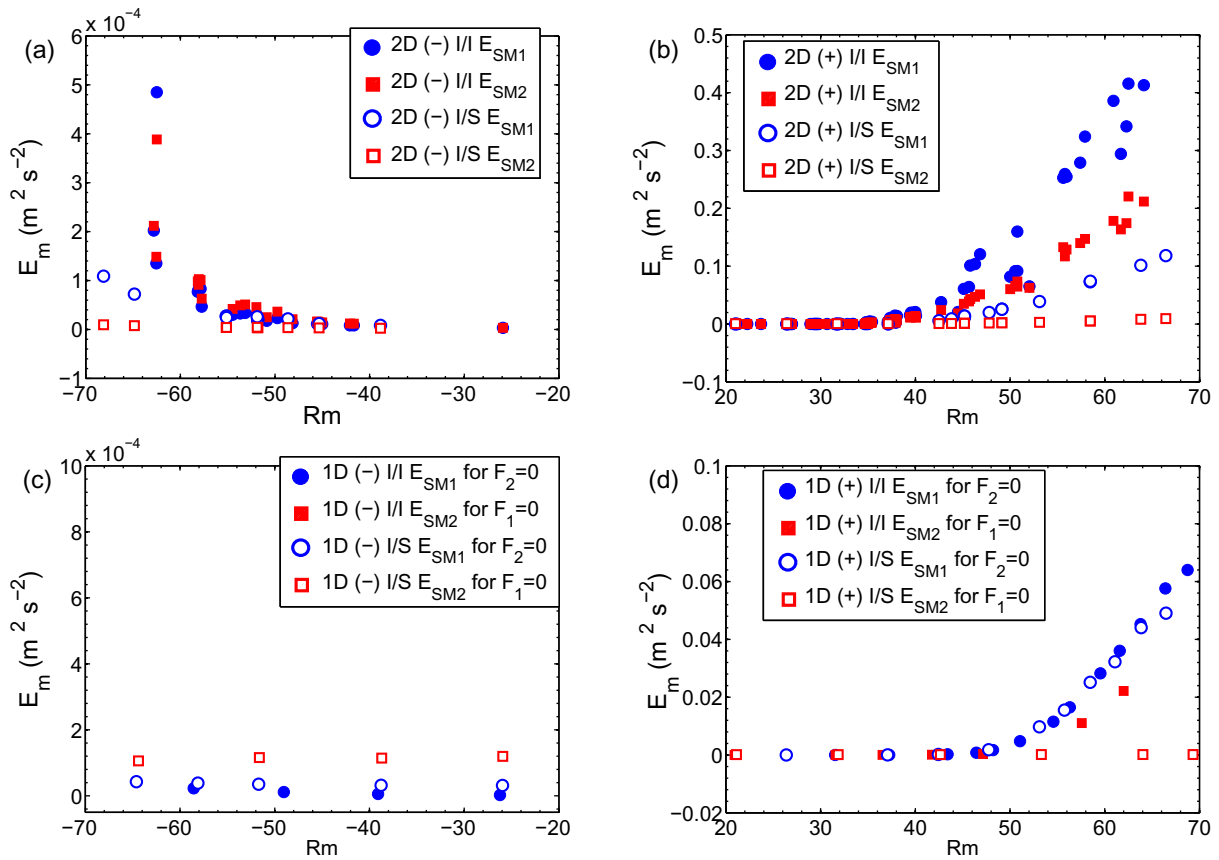


Figure 3. Plot of the averaged mass magnetic energy $E_m = \langle \overline{B^2} \rangle / (\rho \mu_0)$ (in $\text{m}^2 \text{s}^{-2}$) measured with the probes as a function of R_m in four configurations: (a) 2D(-); (b) 2D(+); blue circles: at SM1; red squares: at SM2. (c) 1D(-); (d) 1D(+); blue symbols: at SM1 for $F_2 = 0$ Hz; red symbols: at SM2 for $F_1 = 0$ Hz; filled symbols: with I/I impellers; open symbols: with I/S impellers. Comparing the symbol *colors* informs about the symmetry Left/Right (impeller 1/impeller 2, or $R\pi$); comparing *open/filled* symbols shows the influence of the boundary condition at impeller 2.

figure 3(c)), while in the (+) cases, the dynamo energy is the same when the resting impeller is made of iron or steel (compare open and filled circles in figure 3(d)). This means that the 1D dynamo is insensitive to the electromagnetic boundary condition at the resting impeller side.

Regarding the dynamo onset, one notes by comparing again filled and open symbols in figure 3(b) that the 2D(+) I/I and 2D(+) I/S dynamos have a similar critical magnetic Reynolds number, of the order of 42. The same observation can be made for the 2D(-) dynamos (figure 3(a)), with a higher critical magnetic Reynolds number of the order of 52. Confirming the previous observation on the 1D dynamos, this means that in the 2D(+) and 2D(-) regimes the electromagnetic boundary conditions have a small influence on the dynamo onset, as long as at least one iron impeller is present. Note that the critical magnetic Reynolds numbers are different between 2D(-) and 2D(+), where the fluid motions are very different [8, 20], which confirms the importance of the flow characteristics in the dynamo onset [23].

Table 2. Threshold and symmetry properties of the dynamos at $\epsilon = (R_m - R_{m_c})/R_{m_c} = 0.2$. By convention, we set $R_{m_c} = \pm\infty$ is there if no dynamo at all. NA stands for not available.

Configuration name	R_{m_c}	$\Delta(R\pi)$	$\Delta(\text{Dip})$	$\Delta(\text{Axi})$
I (2D(+)) I/I)	40 ± 2	0.2	0.1	0.11
II (2D(-)) I/I)	-52 ± 2	0.09	0.05	0.2
III (1D(+)) I/I)	50 ± 3	NA	NA	0.1
IV (1D(-)) I/I)	< -65	NA	NA	NA
V (2D(+)) I/S)	42 ± 2	0.7	0.42	0.14
VI (2D(-)) I/S)	-52 ± 2	0.57	0.34	NA
VII (1D(+)) I/S)	I: 50 ± 2 /S: > 70	NA	NA	NA
VIII (1D(-)) I/S)	I: < -65 /S: < -65	NA	NA	NA

3.3. Symmetries

Figure 3 also provides indications of the symmetry properties of the dynamo. Indeed, in the absence of probe number 4, the experimental device is symmetric with respect to a rotation of angle π around an axis perpendicular to the axis of rotation, and in the plane of the probes SM1 to SM3 ($R\pi$ symmetry). A magnetic field symmetric or antisymmetric under the $R\pi$ symmetry should satisfy either $B = R\pi(B)$ (quadrupole-like) or $B = -R\pi(B)$ (dipole-like). In such a rotation, probes 1 and 2 (and impellers 1 and 2) are exchanged, and the conditions for a symmetric or antisymmetric mode with respect to the $R\pi$ symmetry can be written at the probe locations as

$$b_r(\text{SM1}) = \lambda b_r(\text{SM2}), \quad (1)$$

$$b_\phi(\text{SM1}) = -\lambda b_\phi(\text{SM2}), \quad (2)$$

$$b_z(\text{SM1}) = -\lambda b_z(\text{SM2}), \quad (3)$$

where $\lambda = +/ - 1$ for symmetric/antisymmetric modes.

Even if the configuration is not $R\pi$ symmetric, one can decompose the magnetic field into its $R\pi$ symmetric and antisymmetric parts to evaluate the influence of the experimental symmetry on the magnetic field symmetry. Compare then in figure 3 the blue filled circles and red filled squares (for I/I impellers) or the blue open circles and the red open squares (for I/S impellers). In the latter case, the two mean magnetic energies are very different in all configurations. This is a confirmation that the soft-iron and steel impellers play very different roles in the dynamo process and therefore cannot be exchanged by the $R\pi$ symmetry. In the case of I/I impellers, we observe a clear symmetry breaking of the mean magnetic field in the (+) case, in both the 2D (figure 3(b)) and 1D (figure 3(d)) cases.

In contrast, the mean magnetic field is almost symmetric in the 2D(-) case (figure 3(a)). There are several natural ingredients of the $R\pi$ symmetry breaking: the presence of the fourth probes in the plane $\phi = \pi/2$ (SM4), different magnetization in impeller 1, impeller 2, etc. However, it is not clear why these ingredients would play a role in the (+) case and not in the (-) case (note that 2D (-) flow is characterized by much larger hydrodynamic fluctuations than the 2D (+) or the 1D (+)).

Using equations (1)–(3), we may further quantify the importance of the $R\pi$ symmetry breaking and of the deviation from a dipolar magnetic structure through the quantities:

$$\Delta(R\pi) = \frac{\sum_i (|B_i(\text{SM1})| - |B_i(\text{SM2})|)}{\sum_i (\sqrt{B_i(\text{SM1})^2} + \sqrt{B_i(\text{SM2})^2})},$$

$$\Delta(\text{Dip}) = \frac{\sum_i (B_i(\text{SM1}) + \lambda_i B_i(\text{SM2}))}{\sum_i (\sqrt{B_i(\text{SM1})^2} + \sqrt{B_i(\text{SM2})^2})},$$
(4)

where the sum runs over the three components of the magnetic field, and $(\lambda_1, \lambda_2, \lambda_3) = (1, -1, -1)$ so that $\Delta(\text{Dip})$ represents a non-dimensional norm of $B + R\pi(B)$ (which should be 0 for a dipole). The results are presented in table 2 for a given distance to threshold $\epsilon = (R_m - R_{m_c})/R_{m_c} = 0.2$. We also report the deviation from axisymmetry, computed as

$$\Delta(\text{Axi}) = \frac{\sum_i (B_i(\text{SM3}) - B_i(\text{SM4}))}{\sum_i (\sqrt{B_i(\text{SM3})^2} + \sqrt{B_i(\text{SM4})^2})},$$
(5)

which should be zero for a perfectly axisymmetric field in the plane of the probes SM3 and SM4.

From these results, one finds that the 2D(+) I/I and the 2D(−) I/I dynamos (with two rotating iron impellers) are quite close to an axisymmetric dipole. The 2D(−) dynamo is more dipolar and $R\pi$ symmetric and less axisymmetric than the 2D(+) dynamo. In contrast, as expected from the configuration asymmetry, the 2D(+) and (−) I/S dynamo, with one rotating steel impeller and one rotating iron impeller, are quite far from the $R\pi$ symmetry (almost 50%) and from a dipolar structure (20–40%), while still being reasonably axisymmetric. The axisymmetry of the observed dynamos is a strong indication that the mean flow is not the main generator of the corresponding dynamo, since it would favor an $m = 1$ mode, with $R\pi$ symmetry in all cases [23]. When only one iron impeller is rotating (1D(+) I/I dynamo), the corresponding dynamo is also quite axisymmetric, confirming the above observation.

3.4. Dipole self-similarity with the distance to the threshold

In section 3.3, we have seen that the stationary dynamo modes generated using two soft-iron impellers are quite close to a dipolar structure. It is therefore interesting to focus on the B_z component of the field, and to study its evolution with distance to threshold. This is done in figure 4 for the 2D(+) I/I, the 2D(−) I/I, the 2D(+) I/S and the 1D(+) I/I dynamos, by monitoring the time-averaged radial profile of $B_z/\sqrt{\langle B^2 \rangle}$ for increasing values of $\epsilon = (R_m - R_{m_c})/R_{m_c}$. When only one iron impeller is rotating (1D(+) I/I and 2D(+) I/S dynamos), we observe a change in the shape of the profile across the dynamo threshold (change of concavity). When two iron impellers are rotating, the concavity of the profile is preserved, but the intensity near the rotation axis is increased. Above the dynamo threshold, the profiles become remarkably self-similar. This is an indication of the existence of a well-established stationary dynamo structure, with the selection of a stable dynamo mode.

3.5. Geometry of the dynamo mode at $\epsilon = (R_m - R_{m_c})/R_{m_c} = 0.2$

Further analysis of the dynamo mode geometry is obtained using the time-averaged radial profiles of the three magnetic field components at the four available probe locations. The distance to threshold is fixed at $\epsilon = 0.2$. The profiles are reported in figure 5.

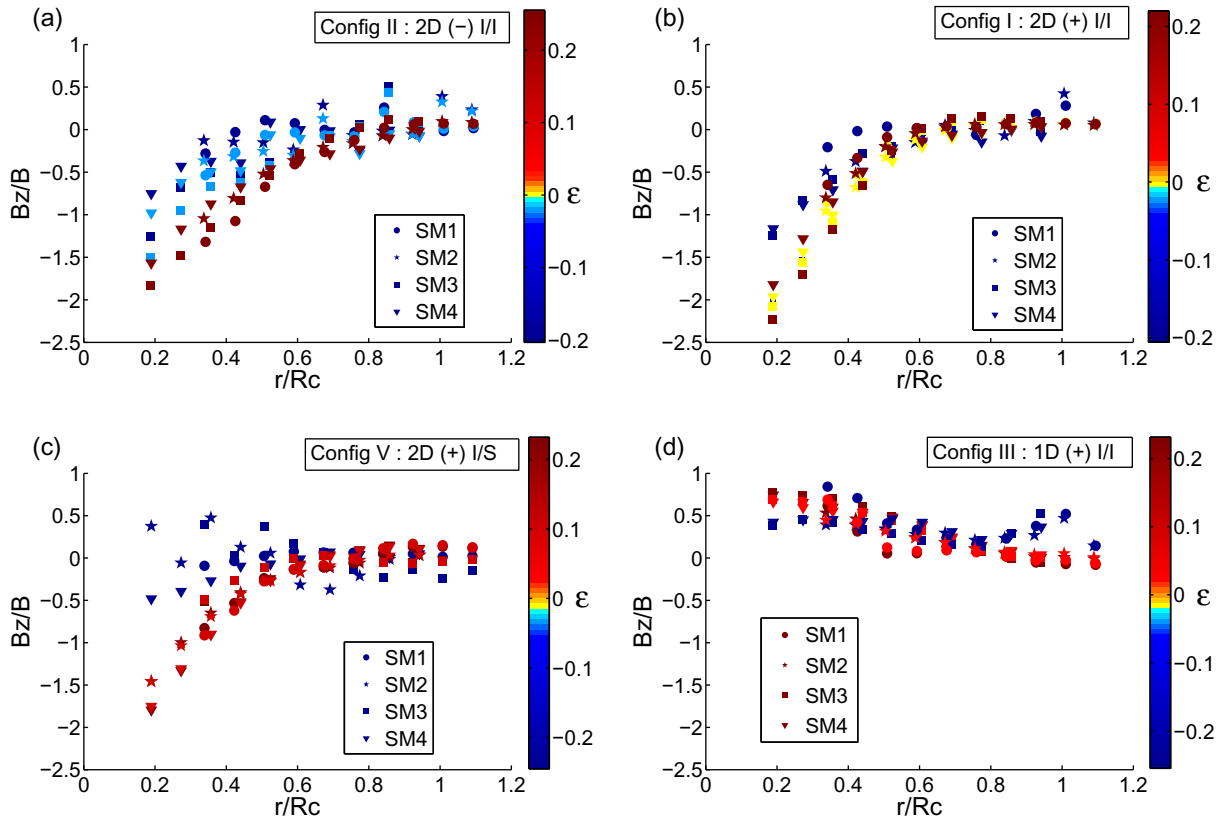


Figure 4. Evolution of the non-dimensional z -components of the magnetic field B_z/B , with $B = \sqrt{\langle B^2 \rangle}$ versus r/R_c (normalized radius) for different values of $\epsilon = (R_m - R_{m_c})/R_m$ in the four configurations: (a) II (2D(-) I/I); (b) I (2D(+) I/I); (c) V (2D(+) I/S); (d) III (1D(+) I/I).

In each case, the comparison between the SM3 (blue) and SM4 (purple) profiles allows one to estimate visually the axisymmetry of the dynamo mode. This axisymmetry is quite well satisfied for all components in all configurations. The $R\pi$ symmetry, given by the comparison between SM1 (red) and SM2 (green), is rather well satisfied for the 2D(+) and (-) I/I dynamo, with $R\pi(B_r) \approx -B_r$, $R\pi(B_\phi) \approx B_\phi$ and $R\pi(B_z) \approx B_z$ (antisymmetric, dipolar mode). In the 2D(+) I/S case and the 1D(+) I/I case, the $R\pi$ symmetry is not satisfied any longer, which is not surprising since the experimental device is not symmetric either.

Comparing now the profiles near the rotating iron impellers (red profiles) in different dynamo configurations, one observes that the 2D(-) I/I dynamo magnetic field (figure 5(a)) is quite different from the magnetic field of the three other cases, in magnitude as well as in shape (for example, the B_ϕ component has an opposite sign with respect to the other three). In contrast, the magnetic modes in the 2D(+) I/I (figure 5(b)), 2D(+) I/S (figure 5(c)) and 1D(+) I/I (figure 5(d)) have very similar shapes. Therefore, the (+) rotation of one iron impeller seems to generate the same magnetic mode in the vicinity of the impeller, whatever the total flow (similarity between 2D(+) I/I and 1D(+) I/I, with very different flows) and whatever the boundary condition at the other impeller (similarity between 2D(+) I/I and 2D(+) I/S). However, the mode generated by the (+) rotation of two iron impellers (figure 5(b)) seems to

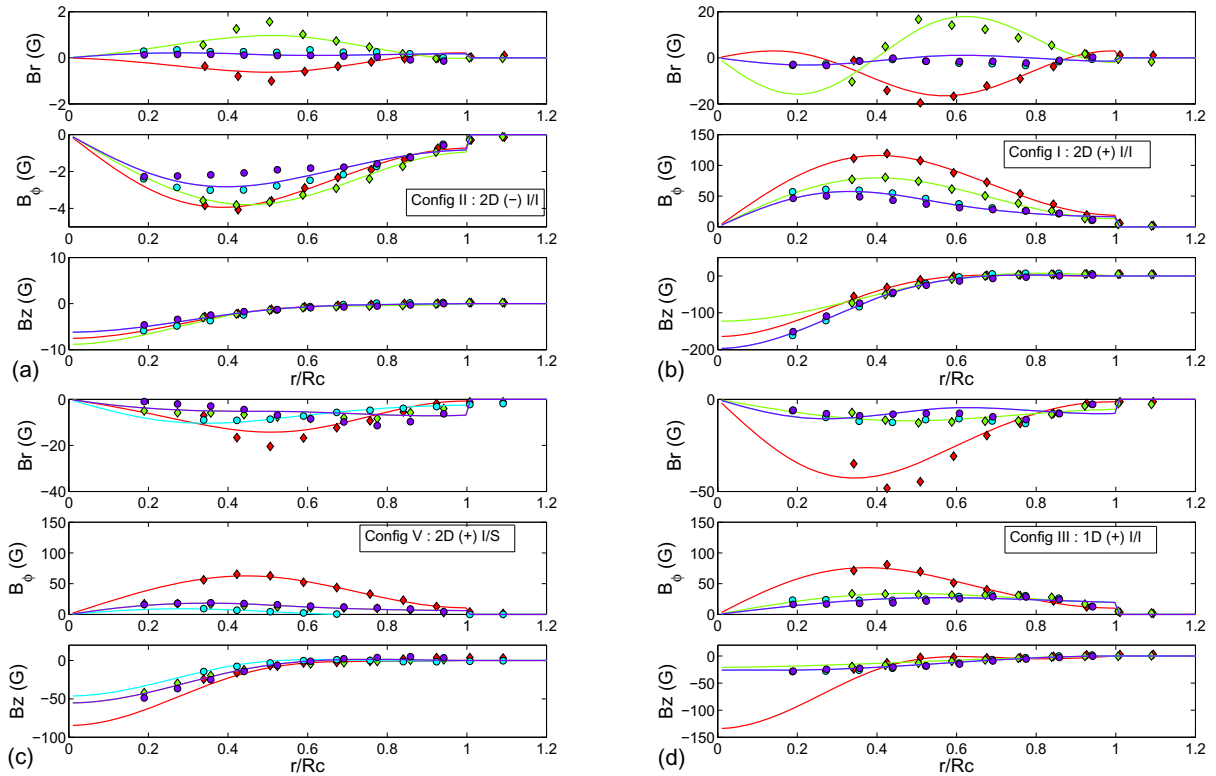


Figure 5. Averaged magnetic profiles for the four probes at $\epsilon = (R_m - R_{mc})/R_{mc} = 0.2$. Red: SM1; green: SM2; blue: SM3; purple: SM4, in the four configurations: (a) II (2D(-) I/I); (b) I (2D(+) I/I); (c) V (2D(+) I/S); (d) III (1D(+) I/I). In the last two cases, the iron impeller is near SM1. The comparison red/green rhombus thus traces the $R\pi$ symmetry (left/right), while the blue/purple circles comparison traces the axisymmetry of the profiles. The symbols are the experimental measurements, and the lines are the interpolations, obtained through the reconstruction method [21]. Note that for comparison convenience, in this figure, we applied the $B \rightarrow -B$ transformation on measures from configuration V.

be about twice as large as the mode generated by the (+) rotation of one iron impeller, when the other impeller is either at rest (figure 5(d)), or rotating but made out of steel (figure 5(c)). These observations cannot rule out a dynamo mechanism in which the 2D(+) I/I dynamo is the superposition of two 2D(+) I/S dynamos or two 1D(+) I/I dynamos. This is discussed in the next section, where we show that in fact nonlinear coupling is essential for the superposition process.

A better insight into the magnetic field spatial structure is obtained by using the reconstruction procedure developed by Boisson and Dubrulle [21] applied to the time-averaged magnetic field profiles measured at the four probes. Considering the number of measurement points and probe locations, we use 30 Galerkin modes, with radial, azimuthal and axial resolutions (3, 1, 5). The reconstructions are shown in figure 5 for profiles at the probe locations and in figure 6 for cuts of the magnetic field in the plane of probes 1–3. One observes that the

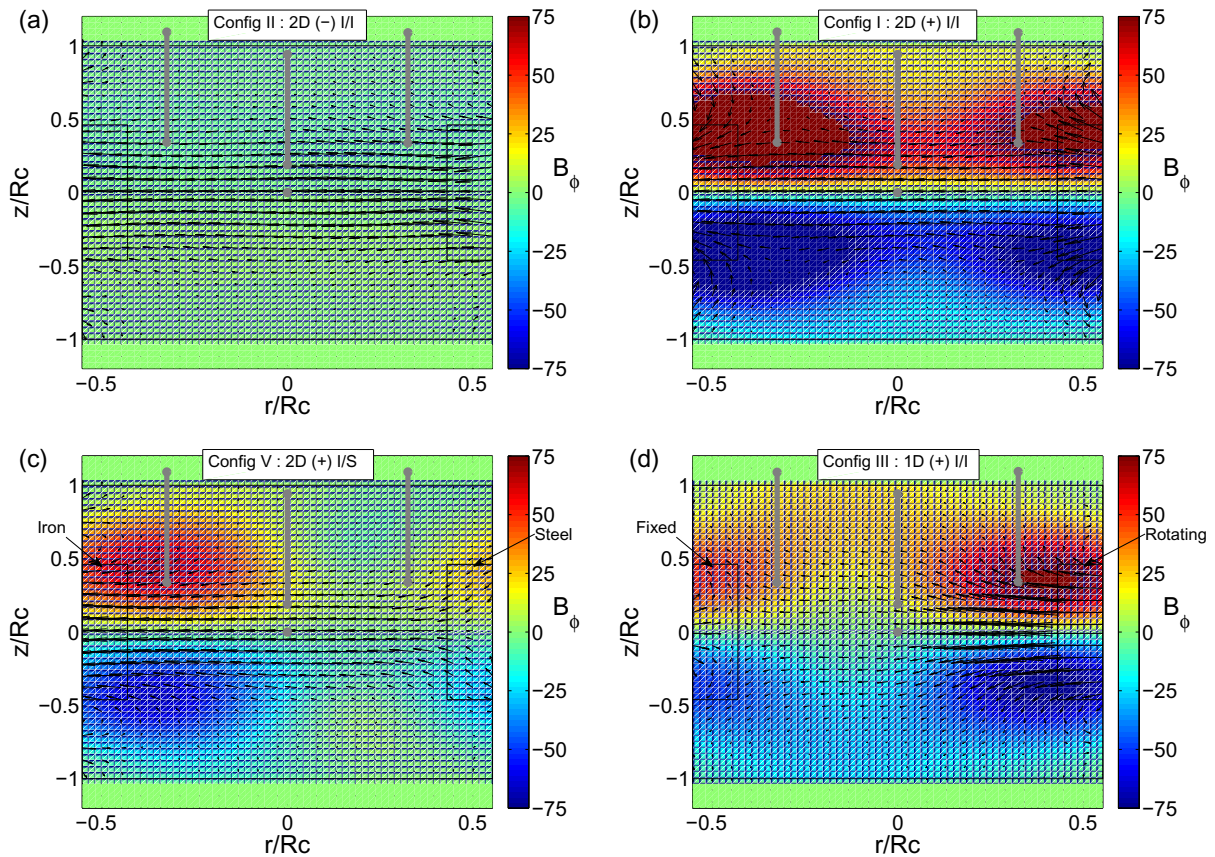


Figure 6. Plot of the averaged magnetic field in the vertical plane containing the probes for $\epsilon = 0.2$. The locations of the blades of two impellers are drawn at the right and at the left extremity. Colors represent the out-of-plane magnetic field component in the four configurations: (a) II (2D(-) I/I); (b) I (2D(+) I/I); (c) V (2D(+) I/S); (d) III (1D(+) I/I). Probes are shown as gray lines.

spatial structure of the dynamo is quite similar in the vicinity of the (+) rotating iron impeller. This is confirmation that in this regime a major part of the dynamo generation is located near the rotating iron impeller. In the 2D(-) I/I case, the dynamo is weaker but the dipolar structure is clearer near the rotation axis as the lower values of B_r and B_θ components suggest. Note that the underlying hydrodynamic flow has stronger large-scale fluctuations in the (-) rotating case than in the (+) case [20, 23]. Analytical [18] and numerical [19] results suggest that the large-scale noise is an impediment to the growth of a dynamo magnetic field. This effect has indeed been observed experimentally in induction regimes [16, 17]. It could also explain why the (-) dynamo is significantly weaker than the (+) dynamo.

4. Discussion and conclusion

In this section, we explore the possibility of describing the 2D(+) I/I dynamo as a nonlinear coupling of two 1D(+) I/I or two 2D(+) I/S dynamos, i.e. from configurations with one rotating

soft-iron impeller. This possibility arises from several observations:

- (i) the dynamo action cannot be obtained unless at least one iron impeller is rotating, with $R_m > 40$ (cf section 3.1 and figure 2);
- (ii) the dynamo action can be absent when two iron impellers are rotating (as in the co-rotating case);
- (iii) the dynamo magnetic mode is rather close to having a dipolar, axisymmetric structure;
- (iv) the 2D(+) I/I dynamo is approximately $R\pi$ antisymmetric;
- (v) the profile of the dynamo magnetic field near the rotating soft-iron impeller is similar in shape in all (+) experiments with at least one rotating iron impeller (cf section 3.5 and figure 5), with a magnitude twice as large when two iron impellers rotate;
- (vi) dynamo properties depend on the sodium flow structure (see section 3.2.3).

Observation (i) suggests that the dynamo generation takes place close to the iron impeller. Because of (ii), we must take into account the possibility of destructive nonlinear coupling. Because of (vi), we can exclude a fully solid dynamo mechanism. Because of (iii), we can exclude a fluid dynamo solely based on the mean velocity, which would produce an equatorial dipole [9, 23].

This is therefore either a semi-fluid dynamo (e.g. α - ω dynamo, with an α process generated by vortices in between the blades [12] or by a turbulence gradient in the impellers vicinity [25, 26] and an ω process generated by the shear close to the impeller and amplified by the high magnetic permeability of the impellers [7]), or a fully fluid dynamo (e.g. α - ω dynamo, with an α process generated by vortices in-between the blades and an ω process generated at the blade interface, where rotation gradients are the largest). Fact (iv) suggests that the two iron impellers play a symmetric role when they both rotate: they are equally responsible for the dynamo action. Deviations from $R\pi$ symmetry may in fact be attributed either to the presence of measuring probes, which break the $R\pi$ symmetry, or to a different magnetization in the left and right iron impellers. This magnetization may lead to asymmetric imperfection of the dynamo action [3].

Observation (v) suggests to describe the 2D(+) I/I dynamo (hereafter labeled B_I) by the coupling of two dynamos with one rotating soft-iron impeller (labeled B_N). The coupling will be using two 1D(+) I/I dynamos ($N = III$) if the fluid structure is not essential but the electromagnetic boundary conditions are, and will be using two 2D(+) I/S ($N = V$) dynamos if the fluid structure is essential and the electromagnetic boundary conditions are not. Because of the two possible different magnetizations in the left and right impellers, the coupling cannot be perfectly symmetric. This suggests therefore to write

$$\begin{aligned} B_I &= \alpha B_N + \beta R\pi(B_N) + B_C \\ &= \tilde{\alpha} Q_N + \tilde{\beta} D_N + B_C, \end{aligned} \quad (6)$$

where $D_N = 0.5(B_N - R\pi(B_N))$ is the antisymmetric part (dipolar) of the field and $Q_N = 0.5(B_N + R\pi(B_N))$ is the symmetric part (quadrupolar) of the field, $\tilde{\alpha}$ and $\tilde{\beta}$ are constants depending on the magnetization difference between the left and right impellers ($\tilde{\alpha} = 0$ for symmetric magnetization of the two impellers) and B_C is a coupling field, describing the potential active effect of the fluid structure in-between the two impellers as well as the effect of nonlinearities in the coupling. If the fluid only serves to propagate current and the coupling is linear, $B_C = 0$. So, we can extract the values of $\tilde{\alpha}_N$ and $\tilde{\beta}_N$ at first order in the coupling by

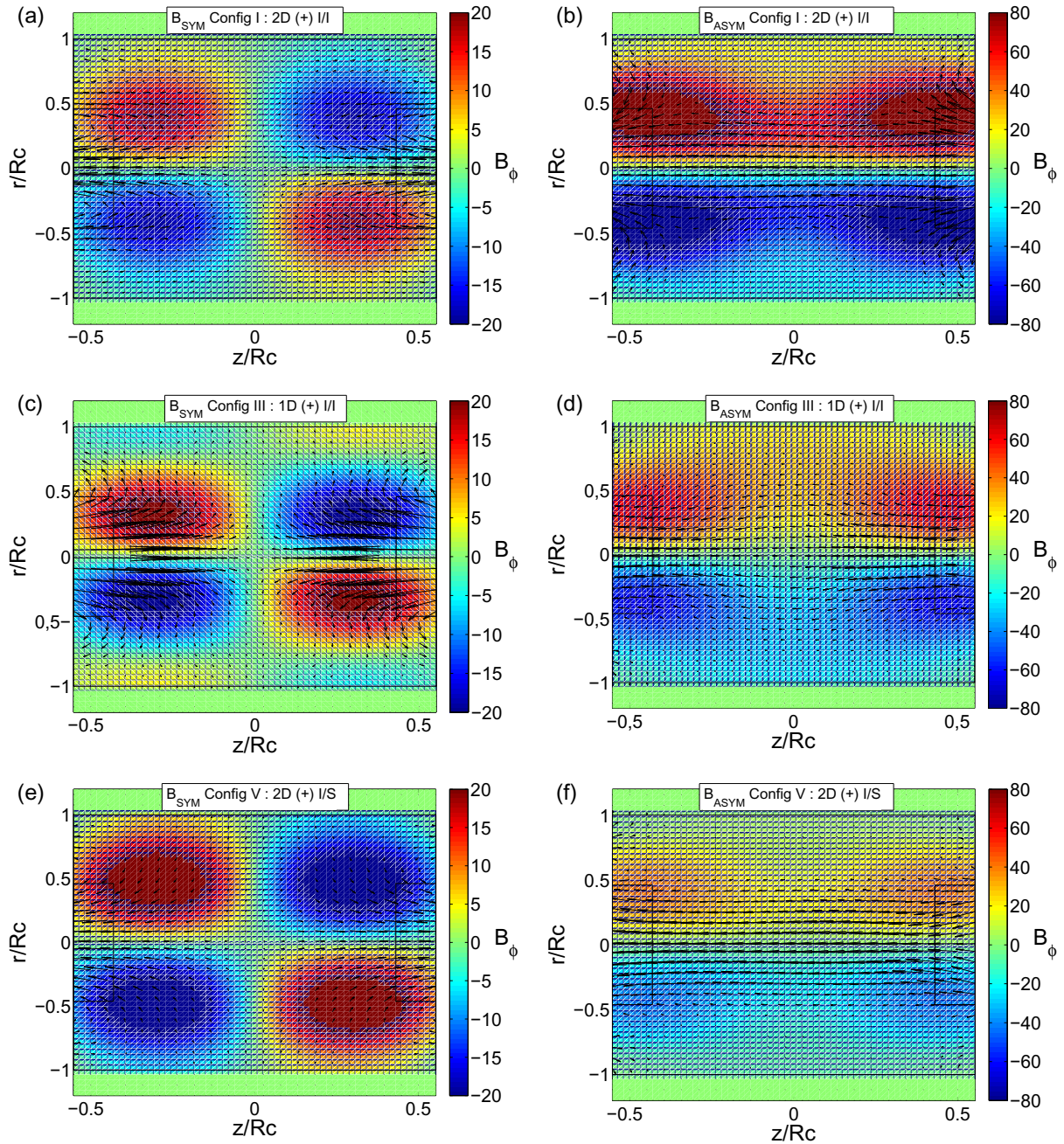


Figure 7. The symmetric part (quadrupole-like, left: (a), (c), (e)) and the antisymmetric part (dipole-like, right: (b), (d), (f)) of the magnetic field in dynamo configurations for $\epsilon = 0.2$; (a) and (b) 2D(+) I/I (configuration I); (c) and (d) 1D(+) I/I (configuration III); (e) and (f) 2D(+) I/S (configuration V). The two impellers are shown at the right and left extremities. Colors correspond to the out-of-plane magnetic field component.

decomposing B_I into its $R\pi$ -symmetric and antisymmetric parts ($B_I = Q_I + D_I$) and plotting Q_I as a function of Q_N and D_I as a function of D_N . For this, we first use the reconstruction technique to compute the dipolar and quadrupolar parts of each field. The result is shown in figure 7.

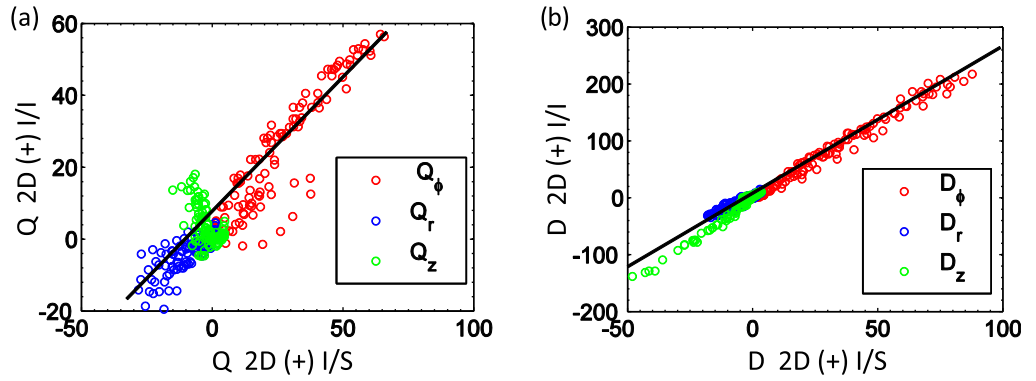


Figure 8. (a) Quadrupolar part of the 2D(+) I/I dynamo versus quadrupolar part of the 2D(+) I/S dynamo at the probe locations for $\epsilon = 0.2$. Blue: Q_r ; red: Q_ϕ ; green: Q_z . (b) Dipolar part of the 2D(+) I/I dynamo versus dipolar part of the 2D(+) I/S dynamo at the probe locations for $\epsilon = 0.2$. Blue: D_r ; red: D_ϕ ; green: D_z .

Overall, one observes a good match in the topology between the 2D(+) I/I case (top) and the 2D(+) I/S case (bottom), while significant differences appear between the 2D(+) I/I case (top) and the 1D(+) I/I case (middle), near the impellers for the quadrupolar part and near the mid-plane for the dipolar part. In order to obtain the most reliable first-order estimation of $\tilde{\alpha}_N$ and $\tilde{\beta}_N$, we restrict ourselves to data at the probe locations \mathbf{x}_p (since the reconstruction is optimized to fit the measurement points, this minimizes possible biases induced by reconstruction far from the probes). We show in figure 8 the resulting evolutions of $Q_I(\mathbf{x}_p)$ as a function of $Q_V(\mathbf{x}_p)$ and those of $D_I(\mathbf{x}_p)$ as a function of $D_V(\mathbf{x}_p)$. The behavior is linear, leading to $\tilde{\alpha} = 0.78$ and $\tilde{\beta} = 2.6$. We have checked that the same plot with $N = \text{III}$ also produces a similar behavior, with a slightly less linear trend, which can be understood as a trace of the poorer match observed in figure 7 between the top and middle plots.

The values of $\tilde{\alpha}_N$ and $\tilde{\beta}_N$ are then used to build the superposition field $B_S = \tilde{\alpha} Q_N + \tilde{\beta} D_N$ and the coupling field $B_C = B_I - B_S$. They are plotted in figure 9, for comparison with the 2D(+) I/I field plotted in figure 6. One sees that the superposition field is closer to the 2D(+) I/I field for the case 2D(+) I/S, resulting in a smaller coupling field. For 1D(+) I/I, the superposition field deviates, with differences more pronounced near the impellers and in the mid-plane shear layer. This is an indication that if the fluid structure plays a role, it is mainly at the location where the turbulence and therefore the momentum transfer are the highest. To detect a possible Reynolds number dependence, we also plot in figures 9(e) and (f) the energy of the coupling field B_C^2 as a function of the distance to the threshold ϵ , as well as the energy of the 2D(+) I/I dynamo and their ratio. We observe that this ratio remains approximately constant, with a value of the order of 40% for $N = \text{V}$ and 50% in the case of $N = \text{III}$. This independence with respect to the magnetic Reynolds number is an indication that it is either a systematic error (proportional to the initial field energy) or linked with a hydrodynamic process, i.e. the flow structure. Moreover, the lowest coupling energy is obtained by combining two counter-rotating I/S dynamos (configuration V). This shows that the fluid structure is essential for explaining the dynamo structure. A similar study using the 2D(-) case could help distinguish between the two possibilities, but is beyond the scope of the present study, for lack of relevant data.

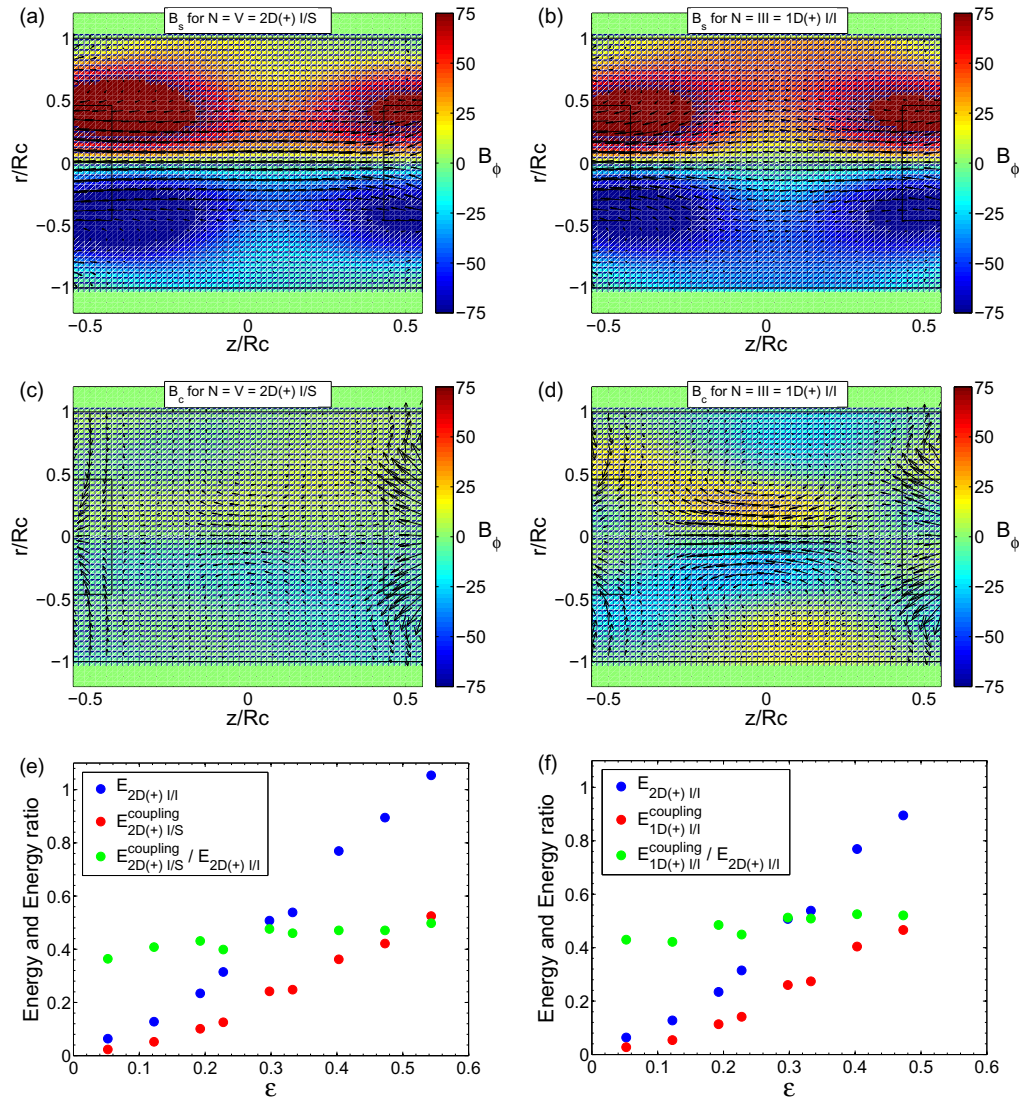


Figure 9. Top: plot of the superposition field $B_S = \tilde{\alpha} Q_N + \tilde{\beta} D_N$: (a) computed using the 2D(+) I/S dynamo; (b) computed using the 1D(+) I/I dynamo. Middle: plot of the coupling field $B_c = B_I - \tilde{\alpha} Q_N - \tilde{\beta} D_N$, where B_I is the 2D(+) I/I dynamo field, Q_N and D_N are the quadrupolar and dipolar parts of the 2D(+) I/S dynamo (c) or the 1D(+) I/I dynamo (d) and $\tilde{\alpha}$ and $\tilde{\beta}$ are the slopes of the fit provided in figure 8. The two impellers are represented at the right and left extremities. Colors represent the out-of-plane magnetic field component. The plots are done at $\epsilon = 0.2$. Bottom: comparison between the normalized energy of the coupling field defined above and the energy of the 2D(+) I/I dynamo, as a function of $\epsilon = (R_m - R_{mc})/R_m$ using the 2D(+) I/S dynamo (e) or the 1D(+) I/I dynamo (f). The energy (blue and red dots) is in $\text{m}^2 \text{s}^{-2}$. Blue: $E_{2D} = \sqrt{\langle B_I^2 \rangle} / (\rho \mu_0)$; red: $E_C = \sqrt{\langle B_C^2 \rangle} / (\rho \mu_0)$; green: E_C / E_I .

Using different observational facts in our experiments, we have therefore proposed a description of the 2D(+) I/I dynamo in terms of three fields: one symmetric field Q , resulting from the symmetric coupling between two dynamo with one rotating soft-iron impeller; one

antisymmetric field D , resulting from the antisymmetric coupling between these two dynamos; one coupling field B_C possibly driven by the hydrodynamic flow structure. This description shares some strong similarities with a theoretical model recently proposed by Petrelis *et al* [22] and Gissinger *et al* [24], in terms of coupling between several modes: a dipolar one, a quadrupolar one [22] plus a hydrodynamic one [24]. Due to the symmetry properties of each component, any normal form description of the dynamics of the three-component interaction will be similar in the two models. However, their interpretation is different: in the present case, the quadrupolar and dipolar modes come from the fluid coupling of two one-impeller fluid dynamos, while in the Petrelis/Gissinger model, they come from dominant kinematic dynamo modes [14].

Acknowledgments

We thank M Moulin, C Gasquet, J-B Luciani, A Skiara, D Courtiade, J-F Point, P Metz, M Tanase and V Padilla for their technical assistance and the other members of the VKS team—B Gallet, C Gissinger, S Fauve, N Mordant and F Pétrélis—for experiments and discussions. This work was supported by grant no. ANR-08-BLAN-0039-02, Direction des Sciences de la Matière et Direction de l'Énergie Nucléaire of CEA, Ministère de la Recherche and CNRS. The experiment was operated at CEA/Cadarache DEN/DTN.

References

- [1] Monchaux R *et al* 2007 Generation of magnetic field by dynamo action in a turbulent flow of liquid sodium *Phys. Rev. Lett.* **98** 044502
- [2] Berhanu M *et al* 2007 Magnetic field reversals in an experimental turbulent dynamo *Europhys. Lett.* **77** 59001
- [3] Monchaux R *et al* 2009 The von Kármán sodium experiment: turbulent dynamical dynamos *Phys. Fluids* **21** 035108
- [4] Berhanu M 2009 Bistability between a stationary and an oscillatory dynamo in a turbulent flow of liquid sodium *J. Fluid Mech.* **641** 217
- [5] Ravelet F *et al* 2008 Chaotic dynamos generated by a turbulent flow of liquid sodium *Phys. Rev. Lett.* **101** 074502
- [6] Berhanu M *et al* 2010 Dynamo regimes and transitions in the VKS experiment *Europhys. J.* **77** 459–68
- [7] Verhille G, Plihon N, Bourgoin M, Odier P and Pinton J-F 2010 Induction in a von Kármán flow driven by ferromagnetic impellers *New J. Phys.* **12** 033006
- [8] Ravelet F private communication
- [9] Ravelet F, Chiffaudel A, Daviaud F and Léorat J 2005 Toward an experimental von Kármán dynamo: numerical studies for an optimized design *Phys. Fluids* **17** 117104
- [10] Stefani F, Xu M, Gerbeth G, Ravelet F, Chiffaudel A, Daviaud F and Léorat J 2006 Ambivalent effects of added layers on steady kinematic dynamos in cylindrical geometry: application to the VKS experiment *Eur. J. Mech. B/Fluids* **25** 894
- [11] Laguerre R, Nore C, Ribeiro A, Léorat J, Guermond J-L and Plunian F 2008 Impact of impellers on the axisymmetric magnetic mode in the VKS2 dynamo experiment *Phys. Rev. Lett.* **101** 104501
- [12] Pétrélis F, Mordant N and Fauve S 2007 On the magnetic fields generated by experimental dynamos *Geophys. Astrophys. Fluid Dyn.* **101** 289
- [13] Giesecke A, Stefani F and Gerbeth G 2010 Role of soft-iron impellers on the mode selection in the von Kármán-sodium dynamo experiment *Phys. Rev. Lett.* **104** 044503
- [14] Gissinger C 2009 A numerical model of the VKS experiment *Europhys. Lett.* **87** 39002

- [15] Gissinger C, Iskakov A, Fauve S and Dormy E 2008 Effect of magnetic boundary conditions on the dynamo threshold of von Kármán swirling flows *Europhys. Lett.* **82** 29001
- [16] Volk R, Odier P and Pinton J-F 2006 Fluctuation of magnetic induction in von Kármán swirling flows *Phys. Fluids* **18** 085105
- [17] Nornberg M D, Spence E J, Kendrick R D, Jacobson C M and Forest C B 2006 Intermittent magnetic field excitation by a turbulent flow of liquid sodium *Phys. Rev. Lett.* **97** 044503
- [18] Leprovost N and Dubrulle B 2005 The turbulent dynamo as an instability in a noisy medium *Europhys. J. B* **44** 395
- [19] Laval J-P, Blaineau P, Leprovost N, Dubrulle B and Daviaud F 2006 Influence of turbulence on the dynamo threshold *Phys. Rev. Lett.* **96** 204503
- [20] Cortet P-P, Diribarne P, Monchaux R, Chiffaudel A, Daviaud F and Dubrulle B 2009 Normalized kinetic energy as a hydrodynamical global quantity for inhomogeneous anisotropic turbulence *Phys. Fluids* **21** 025104
- [21] Boisson J and Dubrulle B 2011 3D magnetic field reconstruction in VKS experiment through Galerkin transforms *New J. Phys.* **13** 023037
- [22] Pétrélis F, Fauve S, Dormy E and Valet J P 2009 Simple mechanism for reversals of Earth's magnetic field *Phys. Rev. Lett.* **102** 144503
- [23] Pinter A, Dubrulle B and Daviaud F 2010 Kinematic dynamo simulations of von Kármán flows: application to the VKS experiment *Europhys. J. B* **74** 165–76
- [24] Gissinger C, Dormy E and Fauve S 2010 Morphology of field reversals in turbulent dynamos *Europhys. Lett.* **90** 49001
- [25] Rädler K-H and Stepanov R 2006 Mean electromotive force due to turbulence of a conducting fluid in the presence of mean flow *Phys. Rev. E* **73** 056311
- [26] Stepanov R, Volk R, Denisov S, Frick P, Noskov V and Pinton J-F 2006 Induction, helicity and alpha effect in a toroidal screw flow of liquid gallium *Phys. Rev. E* **73** 046310